

# Nanoscale chemical tomography of buried organic–inorganic interfaces in the chiton tooth

Lyle M. Gordon<sup>1</sup> & Derk Joester<sup>1</sup>

Biological organisms possess an unparalleled ability to control the structure and properties of mineralized tissues. They are able, for example, to guide the formation of smoothly curving single crystals or tough, lightweight, self-repairing skeletal elements<sup>1</sup>. In many biominerals, an organic matrix interacts with the mineral as it forms, controls its morphology and polymorph, and is occluded during mineralization<sup>2–4</sup>. The remarkable functional properties of the resulting composites—such as outstanding fracture toughness and wear resistance—can be attributed to buried organic–inorganic interfaces at multiple hierarchical levels<sup>5</sup>. Analysing and controlling such interfaces at the nanometre length scale is critical also in emerging organic electronic and photovoltaic hybrid materials<sup>6</sup>. However, elucidating the structural and chemical complexity of buried organic–inorganic interfaces presents a challenge to state-of-the-art imaging techniques. Here we show that pulsed-laser atom-probe tomography reveals three-dimensional chemical maps of organic fibres with a diameter of 5–10 nm in the surrounding nano-crystalline magnetite ( $\text{Fe}_3\text{O}_4$ ) mineral in the tooth of a marine mollusc, the chiton *Chaetopleura apiculata*. Remarkably, most fibres co-localize with either sodium or magnesium. Furthermore, clustering of these cations in the fibre indicates a structural level of hierarchy previously undetected. Our results demonstrate that in the chiton tooth, individual organic fibres have different chemical compositions, and therefore probably different functional roles in controlling fibre formation and matrix–mineral interactions. Atom-probe tomography is able to detect this chemical/structural heterogeneity by virtue of its high three-dimensional spatial resolution and sensitivity across the periodic table. We anticipate that the quantitative analysis and visualization of nanometre-scale interfaces by laser-pulsed atom-probe tomography will contribute greatly to our understanding not only of biominerals (such as bone, dentine and enamel), but also of synthetic organic–inorganic composites.

Organic scaffolds in biominerals generally comprise a fibrous structural element, for example, collagen in bone<sup>7</sup> or chitin in molluscs and crustaceans<sup>8</sup>. Acidic macromolecules, such as the non-collagenous proteins in bone<sup>9</sup> and Asprich proteins in the bivalve prismatic layer<sup>10</sup>, are usually associated with the fibrous scaffold. Although these proteins may be intrinsically disordered, their charge predisposes them to interact with the forming mineral<sup>11</sup>. They are thought to have a key role in controlling crystal polymorph and orientation. Additionally, ions such as  $\text{Mg}^{2+}$  (refs 12 and 13) and polyphosphates<sup>14</sup> are known to be important modulators of mineralization processes. Consequently, our understanding of biological control over mineral growth and the resulting functional properties depends critically on characterizing buried organic–inorganic interfaces.

Characterization of the organic scaffold frequently requires wet chemical demineralization and drying that can result in structural artefacts and loss of diffusive species. The removal of either mineral or organic material also renders it impossible to analyse the interface between the two. The structural complexity of buried interfaces in a synthetic calcite single crystal with occluded agarose fibres was only

recently demonstrated by scanning transmission electron microscopy (STEM) and tomography<sup>15</sup>. However, even this advanced imaging modality does not reveal the chemical complexity of the sample in terms of the localization of different chemical species in the scaffold or the mineral. Although high-resolution elemental mapping by electron microscopy is in principle possible, resolution and sensitivity are greatly limited by the susceptibility of biological materials to beam damage.

We demonstrate herein that atom-probe tomography (APT), an established technique in metallurgical and semiconductor research<sup>16,17</sup>, is capable of chemical tomography of nanoscale buried organic–inorganic interfaces. In particular, we investigate the nano-crystalline magnetite cap ( $\text{Fe}_3\text{O}_4$ , cubic space group  $Fd\bar{3}m$ ; Fig. 1) of the chiton tooth, which is a classical model system for the study of matrix-mediated mineralization<sup>1</sup>. Chitons (also known as sea cradles) are marine molluscs of the class Polyplacophora. Chiton teeth are arranged in rows along the radula (rasping tongue). Similar to vertebrate teeth, mature chiton teeth consist of a softer core (apatite or iron phosphate) capped by a hard magnetite layer<sup>1</sup>. Depending on the species, the capping may cover the whole tooth or just the leading edge, and other mineral phases (for example, lepidocrocite) may be present. The outstanding fracture toughness and wear resistance of the tooth results from the organic–inorganic interfaces over multiple levels of hierarchy, which deflect and arrest cracks<sup>18</sup>. Remarkably, the radula acts as a conveyor-belt on which an organic matrix scaffold composed of semi-crystalline  $\alpha$ -chitin (poly- $\beta$ -1,4-*N*-acetylglucosamine) and protein is first deposited<sup>19</sup>. As the maturing tooth progresses along the radula (about one row per day), the scaffold is remodelled and filled in with mineral, which occludes the organic matrix in the process. All stages of tooth development are thus present in one animal.

Samples for transmission electron microscopy (TEM) and APT were prepared from polished sagittal cross-sections of teeth of the Eastern Beaded Chiton (*Chaetopleura apiculata*, Fig. 2). Focused ion beam (FIB) lift-out techniques were used to prepare electron-transparent

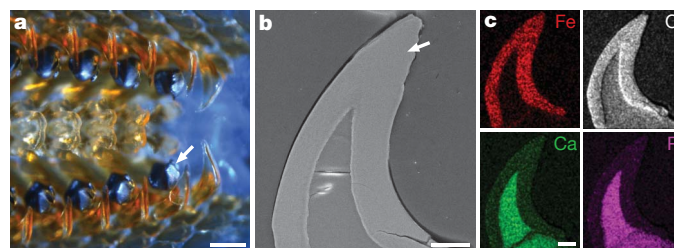


**Figure 1 | Chiton radula and tooth structure.** **a**, Reflected light optical micrograph of the tip of a *C. apiculata* radula, with four rows of fully mineralized teeth (arrow). Scale bar, 200  $\mu\text{m}$ . **b**, SEM image of polished cross-section of a tooth, with approximate site where samples for APT and TEM were extracted (arrow). Scale bar, 50  $\mu\text{m}$ . **c**, Scanning electron microscopy-energy dispersive X-ray spectroscopy (SEM-EDS) elemental maps of cross-section (**b**) showing a Ca/P/O-rich core (apatite) and Fe/O-rich cap (magnetite). Scale bar, 20  $\mu\text{m}$ .

<sup>1</sup>Northwestern University, Department of Materials Science and Engineering, 2220 Campus Drive, Evanston, Illinois 60208, USA.

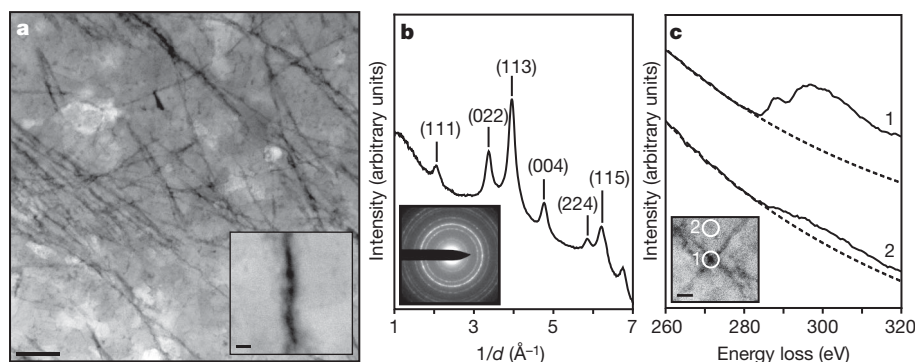


**Figure 2 | Chiton tooth magnetite and occluded organic fibres.** **a**, High-angle annular dark-field STEM image of chiton tooth magnetite showing dark (low- $Z$ ) fibrous structures with a length  $>1\ \mu\text{m}$  and a diameter of  $\sim 5\text{--}10\ \text{nm}$  embedded in the nanocrystalline magnetite (for low angle annular dark field STEM see Supplementary Fig. 7). Scale bar, 100 nm. The inset shows detail of the fibre. Scale bar, 10 nm. **b**, Radially integrated selected-area electron diffraction pattern from the chiton tooth cusp; labelled planes correspond to

samples from the leading edge of the tooth cap. The identity of the mineral (magnetite) was confirmed by selected-area electron diffraction. High-angle annular dark-field STEM reveals numerous dark (weakly scattering) fibrous structures on a bright (strongly scattering) background with dimensions ( $d = 7.6 \pm 2.4\ \text{nm}$ ) similar to those observed in de-mineralized chiton teeth (Fig. 2)<sup>19</sup>. The carbonaceous nature of the fibres was confirmed by carbon K-edge electron energy-loss spectroscopy.

An atom probe is a point projection microscope where, in the presence of a very high electric field, individual or molecular ions sequentially field-evaporate from a sharp tip and are projected onto a two-dimensional position-sensitive detector<sup>16</sup>. The mass-to-charge ratio ( $m/z$ ) and thus the chemical identity of each ion are determined by time-of-flight mass spectrometry using timed picosecond laser pulses to trigger evaporation events. The sequence and location of ions impinging on the detector enables the reconstruction of the three-dimensional structure of the sample. APT analyses volumes of the order of  $10^5\ \text{nm}^3$  with subnanometre spatial resolution<sup>16</sup>. The recent development of ultraviolet laser pulsing greatly increases the scope of the technique, to include high-resistivity materials and organics.

In APT mass spectra of samples from the chiton tooth cusp, magnetite-derived iron, oxygen and iron oxide molecular ions prevail (Table 1), similar to spectra of geological magnetite (Supplementary Fig. 2 and ref. 20). As is typical for oxides, about 25% of the oxygen evaporates as  $\text{O}_2^{2+}$ , which cannot be differentiated from  $\text{O}^+$  (refs 20–22). The measured Fe/O ratio for both the biological ( $0.97 \pm 0.15$ ) and geological magnetite ( $1.13 \pm 0.08$ ) is thus higher than the theoretical value of 0.75. APT mass spectra also contain molecular fragments with  $m/z$  values corresponding to C/N/O-containing ions (Table 1 and Fig. 3), which are not present in spectra of geological magnetite. Although ions such as  $\text{C}^+$  and  $\text{C}^{2+}$  are also found in metal carbides, there is no precedence for carbide formation under physiological conditions. In addition, other ions frequently associated with carbides, such as  $\text{C}_n^+$ ,  $\text{C}_n^{2+}$  ( $n > 1$ ) and  $\text{FeC}^+$  were not detected. However, samples prepared from chitin thin films yield a similar series of molecular ions, confirming that these ions originate from the organic scaffold within the tooth (Fig. 3 and Supplementary Fig. 3). While there is some overlap between organic and mineral-derived ions, for example,  $^{12}\text{C}^{16}\text{O}_2^+$  and  $^{56}\text{Fe}^{16}\text{O}_2^{2+}$  at  $m/z \approx 44$ ,

**Table 1 | Atomic and molecular ions identified in chiton teeth from APT mass spectra**

	Identified ions
Magnetite	$\text{O}^+$ , $\text{O}_2^+$ , $\text{Fe}^{2+}$ , $\text{Fe}^+$ , $\text{FeO}^{2+}$ , $\text{FeO}_2^{2+}$ , $\text{Fe}_2\text{O}_3^{2+}$ , $\text{Fe}_3\text{O}_4^{2+}$ , $\text{FeO}_n^+$ , $n = 1\text{--}4$
Organic matrix	$\text{C}^{2+}$ , $\text{C}^+$ , $\text{CO}^+$ , $\text{CO}_2^+$ , $\text{N}^+$ , $\text{NH}^+$ , $\text{NO}^+$ , $\text{NO}_2^+$ , $\text{CNO}^+$
Other ions	$\text{Mg}^{2+}$ , $\text{Na}^+$ , $\text{Mn}^{2+}$ , $\text{MnO}_n^{z+}$ , $n = 1\text{--}3$ , $z = 1, 2$

magnetite. The inset shows the two-dimensional selected-area electron diffraction pattern. **c**, Carbon-K edge electron energy-loss spectra recorded at fibre intersection (1) and off-fibre (2) demonstrate that fibres are carbon-rich and probably correspond to the chitin observed in unmineralized and demineralized chiton teeth. The inset shows the locations where the measurements were acquired. Scale bar, 20 nm.

analysis based on natural isotopic abundances allows identification and quantification (see Supplementary Notes).

Demonstrating the unique sensitivity of APT across the entire periodic table, APT spectra reveal the presence of the light elements sodium and magnesium and trace amounts of manganese. Although the role of Na in biomineralization is not well understood,  $\text{Mg}^{2+}$  has been shown to modulate mineralization processes, and Mg-binding motifs have been identified in acidic proteins<sup>13,23</sup>. Mn, on the other hand, is a highly regulated, essential cofactor in many redox-active enzymes<sup>24</sup> and may play a part in magnetite mineralization.

We used standard reconstruction algorithms to generate three-dimensional tomograms (Fig. 4 and Supplementary Movies 1–3). The organic-matter-derived ions are clearly seen to originate from fibres occluded within the mineral. The total amount of carbon is less than what would be expected from crystalline chitin fibres. This may be a consequence of overlapping peaks in time-of-flight spectra, preferential evaporation, or biological remodelling of fibres during mineralization<sup>25</sup>. Nevertheless, the fibre diameter (5–10 nm) closely resembles the organic fibres observed in STEM images of the mineralized tooth (Fig. 2a). Furthermore,  $\text{Na}^+$  and  $\text{Mg}^{2+}$  clearly co-localize with organic fibres (Fig. 4). Surprisingly, no biologically relevant counter ions (for example, chloride, phosphate, sulphate) could be detected. Given that chitin is neutral (or, if partially deacetylated, slightly positively charged), the most likely scenario is that acidic proteins associated with the chitin scaffold bind the cations. Interestingly, within each fibre there appear to be small domains around which cations cluster (Fig. 4). It is conceivable that these domains correspond to crystalline  $\alpha$ -chitin domains that exclude acidic proteins and the cations associated with these.

Unexpectedly, in some samples fibres only bind  $\text{Na}^+$  (Fig. 4a and Supplementary Movie 1), whereas  $\text{Mg}^{2+}$  is bound exclusively in others (Fig. 4d and Supplementary Movie 3). This is despite the fact that these samples were taken within a few micrometres of each other. Both  $\text{Mg}^{2+}$  and  $\text{Na}^+$  co-localize with fibres in fibre bundles (Supplementary Movie 2 and Supplementary Fig. 6). There are many examples of proteins that selectively bind and/or transport cations; they frequently differentiate between ions based on their ionic radius, preferred coordination geometry, and hard/soft acid/base properties<sup>26</sup>. For example, the so-called DEAD box motif found in some acidic proteins from biominerals has been suggested to have a role in  $\text{Mg}^{2+}$  binding<sup>12</sup>. It is thus conceivable that in the chiton tooth scaffold, chitin-binding proteins with specificity for either  $\text{Na}^+$  or  $\text{Mg}^{2+}$  are assembled with chitin into a fibre that shows selective binding. The cations themselves may be integrated as part of the assembly, or come in at a later stage. Although we cannot yet provide accurate statistics of the relative frequency of Mg- and Na-binding fibres, it is clear that this unprecedented chemical heterogeneity requires the extension of the number of hierarchical levels to

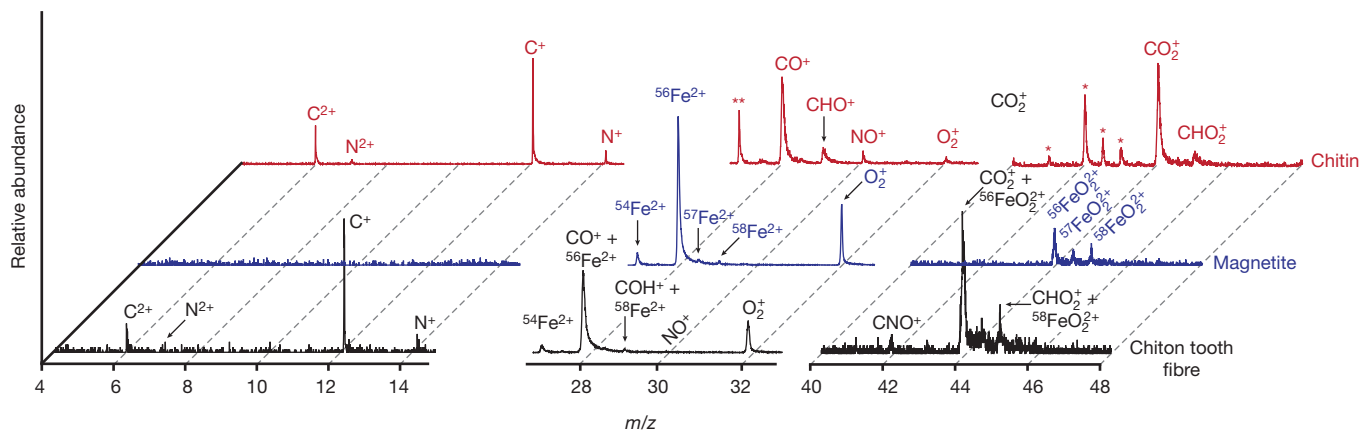


**Figure 3 | APT time-of-flight  $m/z$  spectra.** Typical spectra of organic fibres (black), the surrounding magnetite (blue), and a chitin thin film (red). We note the presence of characteristic chitin-derived atomic and molecular ions ( $C^+$ ,  $C^{2+}$ ,  $N^+$ ,  $N^{2+}$ ,  $CO^+$ ,  $CO_2^+$ ) in the chiton tooth fibre but not in the surrounding magnetite. Spectral overlap between species (for example,  $CO_2^+$  and  $^{56}FeO_2^{2+}$ )

describe the architecture of the chiton tooth accurately. It is possible that similar differences in elemental distributions are present in other biominerals, such as bone or enamel, but have so far been overlooked.

Proximity histograms (proxigrams)<sup>27</sup> that give concentration as a function of distance to the fibre–mineral interface (defined by an isosurface at  $1\text{ C nm}^{-3}$ , Supplementary Fig. 4) reveal that the interface is graded rather than sharp, creating a 2–4-nm-wide region of interpenetrating mineral and organic material (Fig. 4). A graded or rough interface may improve mineral/organic adhesion and enhance mechanical load transfer and toughness. Furthermore, this results in an interface fundamentally different from that observed in single crystals of calcite grown in agarose gels, where high-index planes at the interface create a sharp boundary<sup>15</sup>. Proxigrams also reveal a roughly twofold increase of the manganese concentration in the fibres (Supplementary Fig. 5). This raises the intriguing possibility that Mn-dependent enzymes, some of which may have chitin-binding domains, catalyse the reductive transformation of ferrihydrite to magnetite.

With the fibre backbone being semi-crystalline  $\alpha$ -chitin, it follows that there are crystalline domains and amorphous regions that connect

derived from organics and magnetite can be detected by analysis of natural abundance of Fe isotopes. Species originating from the substrate of the chitin thin film,  $CrO_2^{2+}$  (\*) and  $^{54}Cr^{2+}$  (\*\*), are indicated with asterisks. To account for large differences in relative abundance, each  $m/z$  range is scaled separately.

such domains. It seems reasonable to assume that single strands or loops/coils of amorphous chitin create the rough fibre surface we observe (Fig. 5). The distribution of  $Na^+$  and  $Mg^{2+}$  suggests that chitin-binding proteins with selectivity for either or both cations decorate the fibre surface. They may also be present on the inside of the fibre, but are probably excluded from crystalline domains. Fibre–mineral interactions may be mediated by these cations or direct contacts between side-chain carboxylates, amines, and hydroxyl groups and iron cations or oxy-anions on the mineral surface.

On the basis of this model, it is conceivable that fibres decorated with cations with strongly different charge density (that of  $Mg^{2+}$  is 4–10 times greater than  $Na^+$ , depending on the coordination number) differ in their functional roles. Modulation of colloidal properties such as the  $\zeta$ -potential may be an important way to control fibre self-assembly and maintain the fibre diameter such that mineral overgrowth is not impeded. By inducing counter-ion condensation, the fibre chemistry could also influence where and when nucleation of the mineral phase occurs, similar to what has been proposed for nacre organic matrix<sup>28</sup>. Different strength and geometry of coordinative bonds mediated by

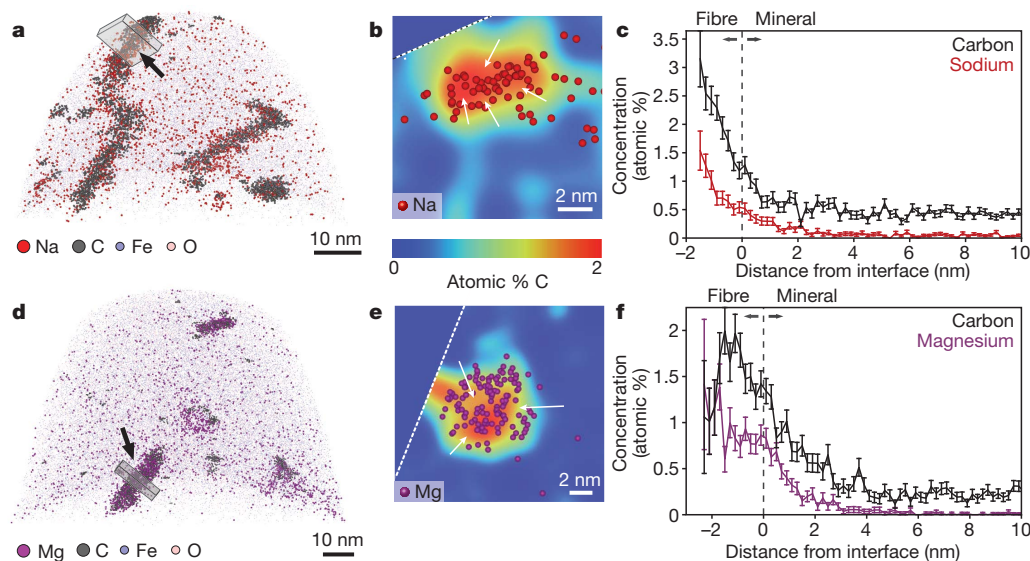


**Figure 4 | Three-dimensional reconstructions and proxigrams.** **a, d**, Two representative samples containing organic fibres that exclusively bind  $Na^+$  (**a–c**) or  $Mg^{2+}$  (**d–f**). For clarity, only about 5% of the Fe/O ions are rendered; the edge of the field-of-view is marked (dashed line in **b**). **b, e**, Overlay of  $Na^+$  (**b**, red spheres) and  $Mg^{2+}$  (**e**, magenta) ion positions on carbon concentration

maps integrated over the boxed regions indicated in **a** and **d**. Some regions of the fibres appear devoid of Na or Mg (arrows). **c, f**, Proximity histograms (error bars,  $\pm 1\sigma$ ) of Na/C (**c**) and Mg/C (**f**) across the organic–inorganic interface of fibres indicated by arrows in **a** and **d**. Interfaces appear graded over 2–4 nm.

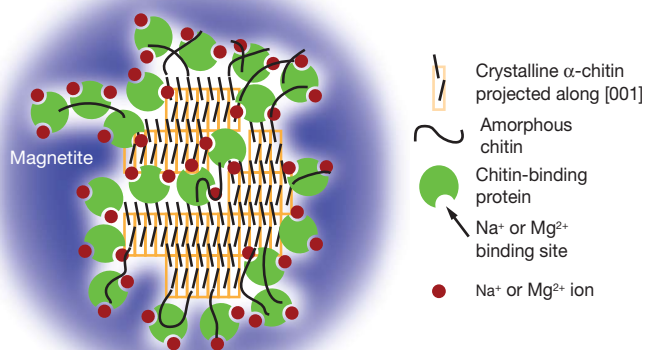


**Figure 5 | Model of a chiton tooth organic fibre.** The backbone of the fibre consists of semi-crystalline  $\alpha$ -chitin. In the crystalline domains, anti-parallel polysaccharide chains are arranged along the [001] direction and are aligned with the fibre axis. Amorphous chitin connects these domains and creates a rough fibre surface. Hypothetical chitin-binding proteins in addition have acidic domains that specifically bind  $\text{Na}^+$  or  $\text{Mg}^{2+}$ . Fibre–mineral interactions may be mediated by these cations and/or acidic, basic or hydroxyl side chains. It is not yet clear whether the magnetite–organic interface involves specific crystallographic planes, is extensively reconstructed, or even strongly disordered (amorphous).

$\text{Na}^+$  and  $\text{Mg}^{2+}$  will affect interactions within the organic matrix, between mineral and organic matrix and/or control the amount of water retained in the final structure. This could modulate the ability of organic matrix molecules to accommodate large strains by elastic uncoiling ('hidden length'), or control energy dissipation during plastic deformation (that is, toughness) through the strength and number of sacrificial bonds<sup>29</sup>. Water is an important lubricant, and the incorporation of  $\text{Mg}^{2+}$  with its tightly bound water molecules may prevent the composite from becoming overly brittle or facilitate reforming sacrificial bonds after deformation, thus contributing to self-healing. Whether the chiton uses these effects to control mineral deposition and properties of the final composite and how we might adapt them to bio-inspired materials synthesis is the subject of our ongoing investigation.

## METHODS SUMMARY

Samples for APT and TEM were prepared using *in situ* FIB lift-out procedures. The chiton tooth samples were prepared from a radula extracted from an Eastern Beaded Chiton (*Chaetopleura apiculata*). Sagittal cross-sections of the teeth for FIB were prepared by chemical fixation, resin embedding, mechanical grinding and polishing and sputter coating with Pt. FIB lift-outs were performed on the leading edge of the magnetite tooth cusp. Geological specimen sections were cut with a diamond saw and mechanically polished. Chitin standards were prepared by dissolving purified chitin in hexafluoroisopropanol and spin-coating on a Cr-coated silicon wafer before coating with Ag. Atom probe tomography was conducted using a LEAP 4000XSi (Cameca). Laser pulsing (wavelength  $\lambda = 355$  nm, 160–500 kHz, 40–75 pJ per pulse) was used to initiate field evaporation. Direct-current potential on the microtip during APT was controlled to maintain a constant evaporation rate (0.0025 or 0.005 ions per pulse). The base temperature of the sample was maintained at 40 or 60 K. The ambient vacuum pressure was maintained below  $10^{-8}$  Pa. The three-dimensional reconstruction of APT data was performed using published algorithms assuming a hemispherical tip shape and an electric-field dependent tip radius<sup>30</sup>.

**Full Methods** and any associated references are available in the online version of the paper at [www.nature.com/nature](http://www.nature.com/nature).

Received 30 July; accepted 18 November 2010.

1. Lowenstam, H. A. & Weiner, S. *On Biomineralization* (Oxford University Press, USA, 1989).
2. Meldrum, F. C. & Colfen, H. Controlling mineral morphologies and structures in biological and synthetic systems. *Chem. Rev.* **108**, 4332–4432 (2008).

3. Weiner, S. Biomineralization: a structural perspective. *J. Struct. Biol.* **163**, 229–234 (2008).
4. Aizenberg, J. in *Nanomechanics of Materials and Structures* (eds Chuang, T. J., Anderson, P. M., Wu, M. K. & Hsieh, S.) 99–108 (Springer, 2006).
5. Fratzl, P. & Weinkamer, R. Nature's hierarchical materials. *Prog. Mater. Sci.* **52**, 1263–1334 (2007).
6. Koch, N. Organic electronic devices and their functional interfaces. *ChemPhysChem* **8**, 1438–1455 (2007).
7. Weiner, S. & Wagner, H. D. The material bone: structure-mechanical function relations. *Annu. Rev. Mater. Res.* **28**, 271–298 (1998).
8. Falini, G. & Fermani, S. Chitin mineralization. *Tissue Eng.* **10**, 1–6 (2004).
9. George, A. & Veis, A. Phosphorylated proteins and control over apatite nucleation, crystal growth, and inhibition. *Chem. Rev.* **108**, 4670–4693 (2008).
10. Gotliv, B. *et al.* Asprich: a novel aspartic acid-rich protein family from the prismatic shell matrix of the bivalve *Atrina rigida*. *ChemBioChem* **6**, 304–314 (2005).
11. Evans, J. S. "Tuning in" to mollusk shell nacre- and prismatic-associated protein terminal sequences. Implications for biomineralization and the construction of high performance inorganic-organic composites. *Chem. Rev.* **108**, 4455–4462 (2008).
12. Wang, D., Wallace, A. F., De Yoreo, J. J. & Dove, P. M. Carboxylated molecules regulate magnesium content of amorphous calcium carbonates during calcification. *Proc. Natl Acad. Sci. USA* **106**, 21511–21516 (2009).
13. Tao, J. H., Zhou, D. M., Zhang, Z. S., Xu, X. R. & Tang, R. K. Magnesium-aspartate-based crystallization switch inspired from shell molt of crustacean. *Proc. Natl Acad. Sci. USA* **106**, 22096–22101 (2009).
14. Omelon, S. J. & Grynaps, M. D. Relationships between polyphosphate chemistry, biochemistry and apatite biomineralization. *Chem. Rev.* **108**, 4694–4715 (2008).
15. Li, H., Xin, H. L., Muller, D. A. & Estroff, L. A. Visualizing the 3D internal structure of calcite single crystals grown in agarose hydrogels. *Science* **326**, 1244–1247 (2009).
16. Kelly, T. F. & Miller, M. K. Atom probe tomography. *Rev. Sci. Instrum.* **78**, 031101 (2007).
17. Seidman, D. N. & Stiller, K. A renaissance in atom-probe tomography. *MRS Bull.* **10**, 717–749 (2009).
18. van der Wal, P., Giesen, H. J. & Videler, J. J. Radular teeth as models for the improvement of industrial cutting devices. *Mater. Sci. Eng. C* **7**, 129–142 (2000).
19. Evans, L., Macey, D. & Webb, J. Distribution and composition of matrix protein in the radula teeth of the chiton *Acanthopleura hirtosa*. *Mar. Biol.* **109**, 281–286 (1991).
20. Kuhlman, K. R., Martens, R. L., Kelly, T. F., Evans, N. D. & Miller, M. K. Fabrication of specimens of metamorphic magnetite crystals for field ion microscopy and atom probe microanalysis. *Ultramicroscopy* **89**, 169–176 (2001).
21. Larson, D. J. *et al.* Analysis of bulk dielectrics with atom probe tomography. *Microsc. Microanal.* **14**, 1254–1255 (2008).
22. Chen, Y., Ohkubo, T., Kodzuka, M., Morita, K. & Hono, K. Laser-assisted atom probe analysis of zirconia/spinel nanocomposite ceramics. *Scr. Mater.* **61**, 693–696 (2009).
23. Marin, F., Luquet, G., Marie, B. & Medakovic, D. Molluscan shell proteins: primary structure, origin, and evolution. *Curr. Top. Dev. Biol.* **80**, 209–276 (2008).
24. Law, N., Caudle, M. & Pecoraro, V. Manganese redox enzymes and model systems: properties, structures, and reactivity. *Adv. Inorg. Chem.* **46**, 305–440 (1998).
25. Evans, L. A., Macey, D. J. & Webb, J. Characterization and structural organization of the organic matrix of the radula teeth of the chiton *Acanthopleura hirtosa*. *Phil. Trans. R. Soc. Lond. B* **329**, 87–96 (1990).
26. Lehn, J. Supramolecular chemistry. *J. Chem. Sci.* **106**, 915–922 (1994).
27. Hellman, O., Vandenbroucke, J., Rüsing, J., Isheim, D. & Seidman, D. Analysis of three-dimensional atom-probe data by the proximity histogram. *Microsc. Microanal.* **6**, 437–444 (2002).
28. Addadi, L., Joester, D., Nudelman, F. & Weiner, S. Mollusk shell formation: a source of new concepts for understanding biomineralization processes. *Chemistry* **12**, 980–987 (2006).
29. Fantner, G. *et al.* Sacrificial bonds and hidden length dissipate energy as mineralized fibrils separate during bone fracture. *Nature Mater.* **4**, 612–616 (2005).
30. Bas, P., Bostel, A., Deconihout, B. & Blavette, D. A general protocol for the reconstruction of 3D atom probe data. *Appl. Surf. Sci.* **87**, 298–304 (1995).

**Supplementary Information** is linked to the online version of the paper at [www.nature.com/nature](http://www.nature.com/nature).

**Acknowledgements** This work was supported in part by the Canadian National Sciences and Engineering Research Council and the US National Science Foundation (DMR-0805313). FIB, SEM and (S)TEM work was performed in the Northwestern University Atomic and Nanoscale Characterization and Experimental Center (NUANCE) supported by NSF-NSEC, NSF-MRSEC, the Keck Foundation, the State of Illinois, and Northwestern University. APT measurements were performed at the Northwestern University Center for Atom Probe Tomography (NUCAPT) supported by NSF-MRI (DMR-0420532) and ONR-DURIP (N00014-0400798, N00014-0610539, N00014-0910781). We thank A. Tayi for help in preparing chitin thin film samples; B. Myers (NUANCE) for help with FIB; D. Isheim (NUCAPT), and D. Lawrence, R. Uffig, T. Prosa and M. Greene (Cameca) for their assistance with APT; and D. Seidman for discussions.

**Author Contributions** L.M.G. and D.J. designed the experiments, analysed the data and prepared the manuscript. L.M.G. performed the experiments.

**Author Information** Reprints and permissions information is available at [www.nature.com/reprints](http://www.nature.com/reprints). The authors declare no competing financial interests. Readers are welcome to comment on the online version of this article at [www.nature.com/nature](http://www.nature.com/nature). Correspondence and requests for materials should be addressed to D.J. ([d-joester@northwestern.edu](mailto:d-joester@northwestern.edu)).

## METHODS

**Consumables.** MgCl<sub>2</sub>, HCl, NaOH, ethanol, NaOCl (VWR); glutaraldehyde, ultra-smooth carbon adhesive tabs (Electron Microscopy Sciences); propylene oxide, Araldite 502, conductive liquid silver paint (Ted Pella); instant all-purpose brush-on cyanoacrylate adhesive (Krazy Glue); EPO-TEK H2OE conductive silver epoxy (Epoxy Technology); CarbiMet II SiC grinding paper, Metadi supreme polycrystalline aqueous diamond polishing suspension, Microcloth polishing cloths (Buehler); Chitin (TCI America); Hexafluoroisopropanol (Sigma-Aldrich); silver pellets, chromium-plated tungsten rods (Kurt J. Lesker Company). Unless otherwise noted, all solutions were prepared in ultrapure water ( $\rho = 18.2 \text{ M}\Omega \text{ cm}$ ) prepared with a Barnstead Nanopure UF+UV ultrapure water purification system (Thermo-Fisher Scientific). Artificial seawater was prepared using Instant Ocean sea salt to a final salinity of  $35 \text{ g l}^{-1}$ .

**Chitin tooth isolation and preparation.** *Chaetopteleura apiculata* (Say, 1834) were acquired live from the Wood's Hole Marine Biological Laboratory. Radulae were extracted by dissection after narcotization of the specimens in aqueous magnesium chloride (0.38 M, 20 min, 15 °C). Radulae were fixed in 3% glutaraldehyde in artificial sea water overnight at 4 °C. Samples were washed once in artificial sea water and water and then dehydrated in a graded ethanol series in water (50, 70, 90 and 100 vol%). Prior to resin infiltration the samples were transferred into propylene oxide. The samples were embedded in Araldite resin and polymerized overnight at 60 °C. The embedded samples were ground using progressively finer grits of SiC grinding paper (400, 600, 800, 1,200 and 2,000 grit) and polished using polycrystalline aqueous diamond polishing suspensions (6, 3, 1.5 and 0.1  $\mu\text{m}$ ). The polished cross-sections were secured to an aluminium stub with cyanoacrylate adhesive, coated with 25 nm of Pt by magnetron sputtering with a turbo-pumped Desk III (Denton Vacuum), then grounded to the stub with conductive liquid silver paint.

**Geological magnetite samples.** Geological magnetite single crystals were acquired from ABCRox and Commercial Crystal Laboratories. The ABCRox sample was cut along the (111) face with a low-speed diamond saw (Buehler Isomet) ground using progressively finer grits of SiC grinding paper (400, 600, 800, 1,200 and 2,000 grit) and polished using polycrystalline aqueous diamond polishing suspensions (6, 3, 1.5 and 0.1  $\mu\text{m}$ ). The polished sample was secured to an aluminium stub using conductive silver epoxy. The Commercial Crystal Laboratories sample was purchased one-side polished with a (100) orientation and then secured to an aluminium stub with a conductive adhesive carbon tab.

**Chitin film purification and preparation.** Crude chitin was purified by adapting previously published protocols<sup>31–33</sup>. The chitin was washed twice in water. The chitin was then stirred with HCl (1.5 M, 6 h, 25 °C), then washed twice with water. The acid-treated chitin was further stirred with NaOH (1.5 M, 3 h, 25 °C) and washed twice with water. The chitin was then treated with NaOCl (10%, 5 min, 25 °C) then washed twice with water. The purified sample was then frozen in liquid nitrogen and lyophilized. The lyophilized chitin was dissolved at  $1 \text{ mg ml}^{-1}$  in hexafluoroisopropanol. The following substrate preparation and spin coating steps were carried out in a nitrogen-filled oxygen-free and water-free glove box to minimize contamination of surfaces with organic materials from the atmosphere. Silicon wafers were first coated with a 28-nm layer of Cr by thermal evaporation (MBraun) at a base pressure below  $10^{-5}$  Pa. Deposit thickness was monitored using a quartz crystal monitor (Inficon). The thermal evaporator was vented with dry nitrogen and the coated substrates were transferred within the glove box to a spin coater (Speciality Coating Systems G3P-B) where they were spin-coated with a chitin film from the hexafluoroisopropanol solution at 3,000 r.p.m. The spin-coated substrates were then coated with 200 nm of Ag at a base pressure below  $10^{-5}$  Pa. The wafer was secured to an aluminium stub with a conductive adhesive carbon tab.

**TEM sample preparation.** TEM lamellae were prepared from a polished cross-section of the chiton tooth following established procedures with a DualBeam scanning electron microscope and FIB instrument (Helios NanoLab, FEI)<sup>34</sup>. First, a strap of platinum (FIB-Pt) was deposited over a region of interest on the polished cross-section using the ion beam (30 kV, 93 pA) to decompose locally an organometallic precursor gas (methyl cyclopentadienyl trimethyl platinum [C<sub>5</sub>H<sub>5</sub>Pt(CH<sub>3</sub>)<sub>3</sub>]). Two trenches were then milled out (30 kV, 6.5 nA) on either side of a 2- $\mu\text{m}$ -thick slice of material. The slice of material was cut free (30 kV, 2.8 nA) from the substrate on three sides, leaving only a small connecting bridge. An *in situ* tungsten nanomanipulator probe (Omniprobe) was attached to the free side of the substrate using FIB-Pt (30 kV, 93 pA). The remaining connection to the substrate was milled away (30 kV, 93 pA) and the probe was retracted with the sample. The sample was then welded to a copper TEM half-grid (Omniprobe) using FIB-Pt and the connection to the probe was milled away (30 kV, 93 pA). The lamella was successively thinned to  $\sim 100 \text{ nm}$  at 30 kV (93 pA) at a  $1\text{--}2^\circ$  incidence angle grazing milling condition. The majority of the surface amorphization and gallium implantation was removed by low-angle milling ( $\sim 7^\circ$ ) at 5 kV and 2 kV (28 pA) to thin the sample to approximately 60–80 nm.

**SEM/TEM methods.** Elemental mapping of polished cross-sections was performed using EDS in the Dual-Beam SEM/FIB operating at 15 kV using a Quantax X-flash silicon drift detector (Bruker AXS). Selected area electron diffraction patterns were acquired using a Hitachi H-8100 operating at 200 kV. High-angle annular dark-field STEM images and electron energy-loss spectra were acquired using a JEOL 2100F operating at 200 kV equipped with a Gatan electron energy loss spectrometer. Electron energy-loss spectroscopy maps were acquired with a dwell time of 1 s per pixel, a probe convergence angle of 10 mrad and a collection angle of 50 mrad. Pre-edge backgrounds were fitted using a power-law function.

**APT sample preparation.** Samples for APT were prepared using the SEM/FIB instrument using established protocols<sup>35–37</sup>. First, a layer of platinum was deposited over a region of interest ( $2 \mu\text{m} \times 25 \mu\text{m}$ ) on the polished cross-section using the ion beam (30 kV, 93 pA). For the geological samples where no sputtered or evaporated metal coating was present a protective 100 nm layer of platinum was deposited first using the electron beam (5 kV, 5.5 nA) before the ion beam was turned on. A wedge of material below the Pt strap was cut out on three sides. The wedge was attached to an *in situ* nano-manipulator (Omniprobe) using FIB-deposited Pt before cutting the final edge free. Segments 1–2- $\mu\text{m}$  wide were cut from the wedge and sequentially affixed to the tops of Si posts in an array (Cameca Scientific Instruments) with FIB-Pt. Each tip was shaped and sharpened using annular milling patterns of increasingly smaller inner and outer diameters<sup>35</sup>. The majority of the amorphized surface region and implanted gallium ions in the tip surface was removed by milling at 5 kV and 2 kV, at 89 pA.

**APT methods.** APT analyses were conducted in a Cameca local-electrode APT (LEAP 4000XSi) using a pulsed laser ( $\lambda = 355 \text{ nm}$ , 160–500 kHz, 40–75 pJ per pulse). The direct-current potential on a microtip during APT was controlled to maintain an evaporation rate of either 0.0025 or 0.005 ions per laser pulse. The base temperature of the microtip was maintained at 40 K or 60 K and the ambient vacuum pressure was  $< 10^{-8}$  Pa.

Three-dimensional reconstruction of APT data was performed using the IVAS atom-probe data visualization and analysis software (Cameca) using published algorithms, assuming a hemispherical tip shape<sup>30,38</sup>. Standard reconstruction parameters were used with an electric-field-dependent radius ( $r$ ). The average evaporation field ( $F_e$ ) of the biogenic chiton tooth magnetite ( $23.5 \text{ V nm}^{-1}$ ) was measured by acquiring either SEM or STEM images of microtips after APT analysis. Atomic volumes of Fe and O for the reconstruction were calculated from published values of ionic radii and the known magnetite crystal structure<sup>39,40</sup>. The atomic volume assigned to oxygen was increased to account for the oxygen deficiency in the measured stoichiometry. Proximity histograms<sup>27</sup> were calculated using a carbon isodensity surface (Supplementary Fig. 4) of one carbon atom per cubic nanometre and then extrapolating to the fibre axis.

**APT three-dimensional renderings.** Three-dimensional renderings of APT data were created in Cameca Integrated Visualization and Analysis Software (IVAS, www.cameca.com/support/ivas.aspx) The carbon containing ions (C<sup>2+</sup>, CO<sub>2</sub><sup>+</sup>, CNO<sup>+</sup>) were only rendered where the local density exceeded  $0.75 \text{ nm}^{-3}$ , owing to the spectral overlap between CO<sub>2</sub><sup>+</sup> and <sup>56</sup>FeO<sub>2</sub><sup>2+</sup> in the magnetite. CO<sup>+</sup> was not rendered, owing to the overlap with <sup>56</sup>Fe<sup>2+</sup>. For clarity, only 5–10% of the background Fe and O ions were rendered.

**APT two-dimensional concentration plots.** Two-dimensional concentration plots were created with a pixel size of 0.1 nm. The three-dimensional grid voxel size was  $0.2 \text{ nm} \times 0.2 \text{ nm} \times 0.2 \text{ nm}$  and the delocalization parameters were 2.5 nm in  $x$  and  $y$  and 1.25 nm in  $z$ . The edge of the field of view (where the ions from the tip hit the local electrode) is marked with a white dashed line. The concentrations were averaged over a 3-nm-thick region.

- Tsai, G. J., Su, W. H., Chen, H. C. & Pan, C. L. Antimicrobial activity of shrimp chitin and chitosan from different treatments and applications of fish preservation. *Fish. Sci.* **68**, 170–177 (2002).
- Li, J., Revol, J. F. & Marchessault, R. H. Effect of degree of deacetylation of chitin on the properties of chitin crystallites. *J. Appl. Polym. Sci.* **65**, 373–380 (1997).
- Sikorski, P., Hori, R. & Wada, M. Revisit of chitin crystal structure using high resolution X-ray diffraction data. *Biomacromolecules* **10**, 1100–1105 (2009).
- Giannuzzi, L. A. & Stevie, F. A. A review of focused ion beam milling techniques for TEM specimen preparation. *Micron* **30**, 197–204 (1999).
- Miller, M. K., Russell, K. F. & Thompson, G. B. Strategies for fabricating atom probe specimens with a dual beam FIB. *Ultramicroscopy* **102**, 287–298 (2005).
- Thompson, K. F. *et al.* *In situ* site-specific specimen preparation for atom probe tomography. *Ultramicroscopy* **107**, 131–139 (2007).
- Miller, M. K., Russell, K. F., Thompson, K., Alvis, R. & Larson, D. J. Review of atom probe FIB-based specimen preparation methods. *Microsc. Microanal.* **13**, 428–436 (2007).
- Miller, M. K. *Atom Probe Tomography: Analysis at the Atomic Level* 139–153 (Plenum, 2000).
- Shannon, R. Revised effective ionic radii and systematic studies of interatomic distances in halides and chalcogenides. *Acta Crystallogr. A* **32**, 751–767 (1976).
- Fleet, M. The structure of magnetite. *Acta Crystallogr. B* **37**, 917–920 (1981).